



Relative contributions of global warming, AMO and IPO to the land precipitation variabilities since 1930s

Li Tao^{1,2} · X. San Liang^{1,3} · Lin Cai¹ · Jiuwei Zhao⁴ · Meng Zhang¹

Received: 27 May 2020 / Accepted: 11 December 2020

© The Author(s), under exclusive licence to Springer-Verlag GmbH, DE part of Springer Nature 2021

Abstract

The relative contributions of ocean modes to the JJA and DJF land precipitation variabilities during 1934–2015 are investigated using a variety of statistical and dynamical system methods, i.e., singular value decomposition (SVD), multivariate linear regression, and information flow analysis. Through SVD analysis for the tropical land precipitation and sea surface temperature (SST), three ocean modes are found to most affect the trend and interdecadal variation of the land precipitation. They are the global warming (GW) mode, Atlantic Multidecadal Oscillation (AMO) and Interdecadal Pacific Oscillation (IPO). GW contributes dominantly to the tropical land rainfall variability in both the JJA and DJF seasons. In JJA (DJF), AMO (IPO) plays a role only secondary to GW. Locally, within the thin latitude bands 10° S–10° N, 50° N–60° N and 40° S–50° S, GW, AMO and IPO are of equal importance in JJA; outside these bands, in the same season the first two dominate. In the band 10° N–40° N, IPO is the primary contributor in DJF, but outside it, GW dominates. Also, these contributions differ geographically from continent to continent. These results have been substantiated in the application of information flow analysis, a recently developed method in physics for the inference of causality between dynamical events. In terms of information flow, we have presented the regions of sensitivity to the three modes. Also presented are a number of ECHAM model experiments, which, besides verifying the above results, show for the first time that the Indian Ocean is pivotal in having AMO and IPO in effect in causing the precipitation variabilities.

Keywords Land precipitation · Global warming · Atlantic multidecadal oscillation · Interdecadal pacific oscillation · relative contribution

Electronic supplementary material The online version of this article (<https://doi.org/10.1007/s00382-020-05584-w>) contains supplementary material, which is available to authorized users.

✉ Li Tao
taoli@nuist.edu.cn

¹ School of Atmospheric Sciences, Nanjing University of Information Science and Technology, Nanjing 210044, Jiangsu, China

² Key Laboratory of Meteorological Disaster, Ministry of Education (KLME), Nanjing University of Information Science and Technology, Nanjing 210044, Jiangsu, China

³ School of Marine Sciences, Nanjing University of Information Science and Technology, Nanjing 210044, Jiangsu, China

⁴ Division of Environmental Science and Engineering, Pohang University of Science and Technology (POSTECH), Pohang, Gyeongbuk 790-784, South Korea

1 Introduction

In a background of global warming (GW), future precipitation variations are expected to follow a ‘rich get richer’ pattern because of the effect of moisture changes in the atmosphere (Chou and Neelin 2004; Held and Soden 2006; John et al. 2009). However, Greve et al. (2014) used more than 300 combinations of hydrological datasets during 1948–2005 to investigate the wetting and drying trends in different regions, and found that only 10.8% of the global land areas were in a robust ‘wet gets wetter, dry gets drier pattern’. The coupled model simulations also have revealed a precipitation scenario different from the wet-get-wetter pattern (Xie et al. 2010). Besides these, it has also shown that precipitation trends are more geographically dependent; for example, increase near the equator, decrease in the subtropical subsidence regions, and a smaller but more consistent increase in mid-latitudes have been observed (e.g. Allen and Ingram 2002; Zhang et al. 2007; Gu and Adler 2015).

Many studies attributed the above precipitation variabilities to the increasing concentrations of CO₂ and other greenhouse gases (GHGs) in the atmosphere (e.g. Dai et al. 1997; Allen and Ingram 2002; Emori and Brown 2005).

Besides this, the role of sea surface temperature (SST) on precipitation variabilities has been emphasized in many studies. Particularly, the change observed in some regional precipitation seems to result from a combined influence of the global warming and oceanic decadal variability (e.g. Mohino et al. 2011; Gu and Adler 2013; Gu and Adler 2015; Dong and Dai 2015; McCabe et al. 2004; Xie et al. 2010). For example, the positive (negative) phase of the Atlantic Multi-Decadal Oscillation (AMO; Kerr 2007; Kushnir 1994; Schlesinger and Ramankutty 1994) is believed to enhance (suppress) the precipitation over Sahel, and suppress (enhance) that over Guinea Gulf (Folland et al. 1986; Knight et al. 2006; Zhang and Delworth 2006; Mohino et al. 2011); the positive AMO phase also contributes to the drought over northeast Brazil during the boreal winter, and the wetting over central America during the boreal summer (Zhang and Delworth 2006; McCabe et al. 2004) suggested that about 70% of the temporal variability in drought frequency over the continental U.S. during 1900–1999 could be explained by PDO, AMO, and the North Hemisphere temperature. The correlation between AMO and drought frequency reveals a consistent positive pattern over the central U.S.

The Interdecadal Pacific Oscillation (IPO; Mantua et al. 1997; Zhang et al. 1997; Deser et al. 2004; Salinger et al. 2001; Power et al. 1999) is another mode of oceanic decadal variability which affects land precipitation in many regions. Gu and Adler (2013) suggested that the observed linear change in global mean precipitation during 1988–2010 might be accounted for jointly by the global mean surface warming and Pacific decadal Oscillation (PDO)—hence IPO. They (Gu and Adler 2015) also suggested that PDO/IPO and AMO both play important roles in the precipitation variations in the middle and high latitudes of the Northern Hemisphere. Positive correlations exist between the IPO index and the regional precipitations over Southwest U.S., Argentina, and parts of Europe and Asia, whereas negative correlations are found over southern and western Africa, eastern Australia, southeastern and northeastern Asia (Dong and Dai 2015; Dai 2013). It was also reported (Yang et al. 2017) that IPO plays a dominant role in the interdecadal variation of the north-south precipitation anomaly dipole over eastern China, and that the dipole pattern is enhanced when the IPO and AMO are in opposite phases.

Though the SST-driven variability of precipitation is the subject of numerous studies, the relative contributions of GW, AMO, and IPO have not yet been quantified directly from observation. To our best knowledge, such quantification has only been exercised through numerical modeling. However, the limitations of models in reproducing

precipitation variabilities are well known. In this study, instead, we approach the problem directly from the reanalysis data. Specifically, we will identify the dominant modes affecting on the trend/decadal variation of land precipitation in different seasons, and quantitatively assess their relative contributions using a variety of methods. Particularly, we will employ a recently developed causal inference method, i.e., the information flow analysis developed by Liang (2014) to unravel the cause-effect relation between time series, to identify the regions where GW, AMO or IPO can significantly affect. These identifications/inferences are then verified in numerical experiments with the atmospheric general circulation model ECHAM 4.6. As we will see, besides the verification, the numerical experiments reveal to us that Indian Ocean is pivotal in that it cooperates with the Pacific and Atlantic to influence the land precipitation variability.

The remainder of the paper is organized as follows. Below we first describe the data and methods. In Sect. 3.1, SST modes are identified that contribute to the trend/decadal variabilities of the land precipitation. Their relative contributions are then assessed. As a verification, in Sect. 3.5 numerical experiments are conducted and results are presented. A summary is given in Sect. 4.

2 Data and methods

2.1 Data

The monthly land precipitation dataset used in this study is obtained from the Climate Research Unit Time Series (CRU TS 2.1). The dataset has a horizontal resolution of $0.5^\circ \times 0.5^\circ$ and is available from 1901 (Harris et al. 2014). Because the data over some regions (e.g. northern Africa) are set to climatology monthly means before 1933, the analysis period of this study is set from 1934 to 2015 to ensure the data reliability. Another monthly land precipitation dataset from Global Precipitation Climatology Centre (GPCC) Full Data Reanalysis V2018 are also used to verify the results (Schneider et al. 2014). It has a horizontal resolution of $1^\circ \times 1^\circ$ for the period of 1934–2015, based on the quality-controlled data from 67,200 stations world-wide that feature record durations of 10 years or longer.

The SST dataset is from the monthly Hadley Center sea ice and SST dataset (HadISST; Rayner et al. 2011). Another SST dataset from Extended Reconstructed Sea Surface Temperature v3 (ERSSTv3; Smith et al. 2008) is also used to verify the results. HadISST is primarily based on observations from the UK Met Office, whereas ERSSTv3 is based on the International Comprehensive Ocean–Atmosphere Data Set (ICOADS) SST anomalies. Both have a global coverage but with different horizontal resolutions ($1^\circ \times 1^\circ$ for HadISST and $2^\circ \times 2^\circ$ for ERSSTv3).

The monthly National Centers for Environmental Prediction (NCEP)–National Center for Atmospheric Research (NCAR) atmospheric reanalysis dataset (Kalnay et al. 1996) are also used as observations for the purpose of model validation.

As we will see soon, the ocean modes that dominate the precipitation variabilities are GW, AMO, and IPO. We need

the time series of their indices for the purpose of this study. The GW time series is derived from the yearly global SST averaged between the latitude 45° S and 60° N (Mohino et al. 2011), which is a good approximation for the observed warming signal in global ocean; it is shown in Figs. 1c and 2c. The area beyond the band is excluded because of the poor SST data coverage (Baines and Folland 2007). As the

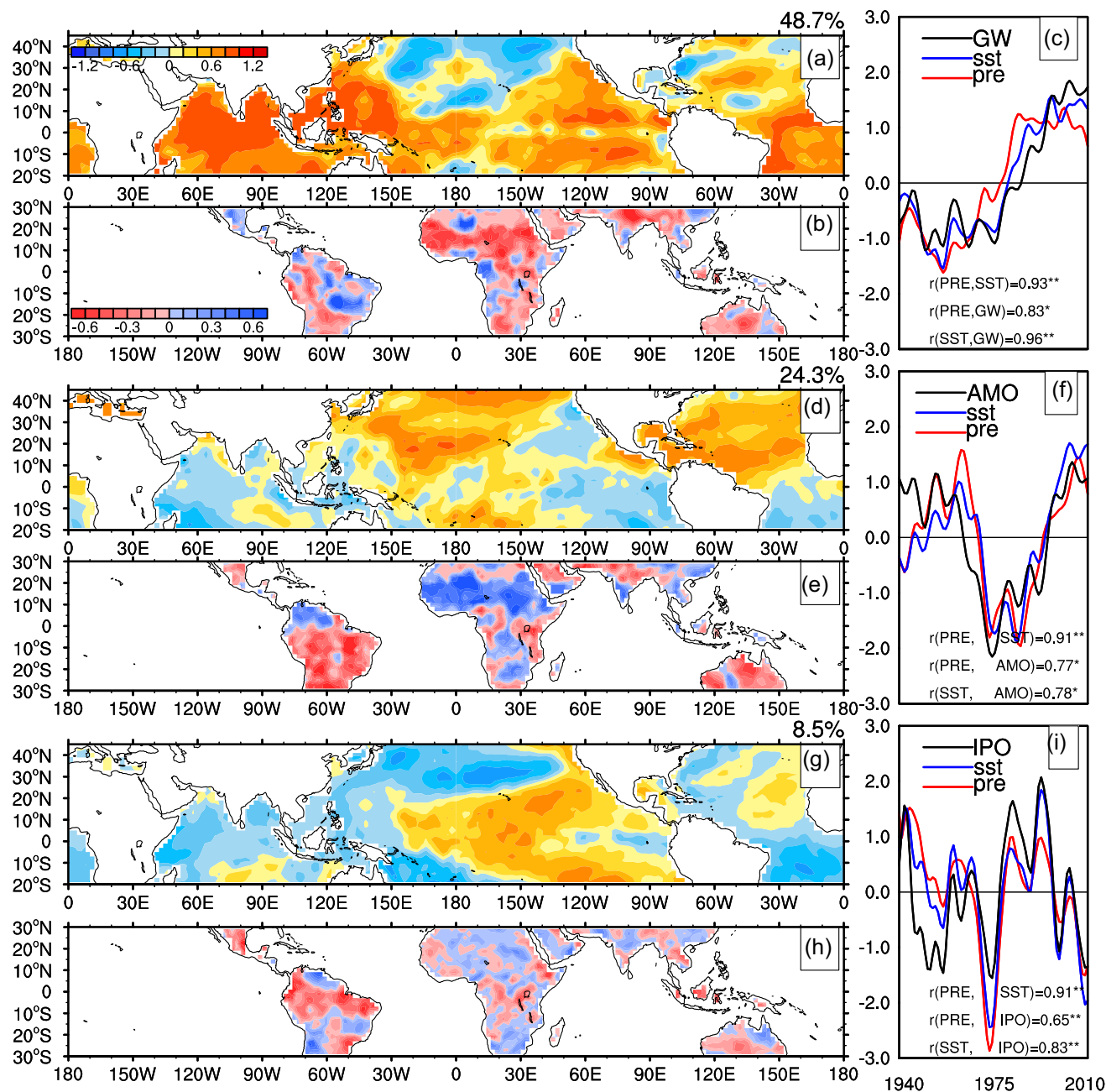


Fig. 1 The first three SVD modes between the SST (20° S–45° N) from HadISST and the tropical land precipitation from CRU during the JJA seasons of 1934–2015. (a, d, g) are the first three spatial patterns of SST; (b, e, h) are those of land precipitation. The normalized SVD time series of SST (blue lines) and precipitation (red lines) are

shown in (c, f, i). The black lines in (c, f, i) are for GW, AMO and IPO. The correlation coefficients (r) with * are statistically significant at the 5% level, and those with ** are statistically significant at the 1% level

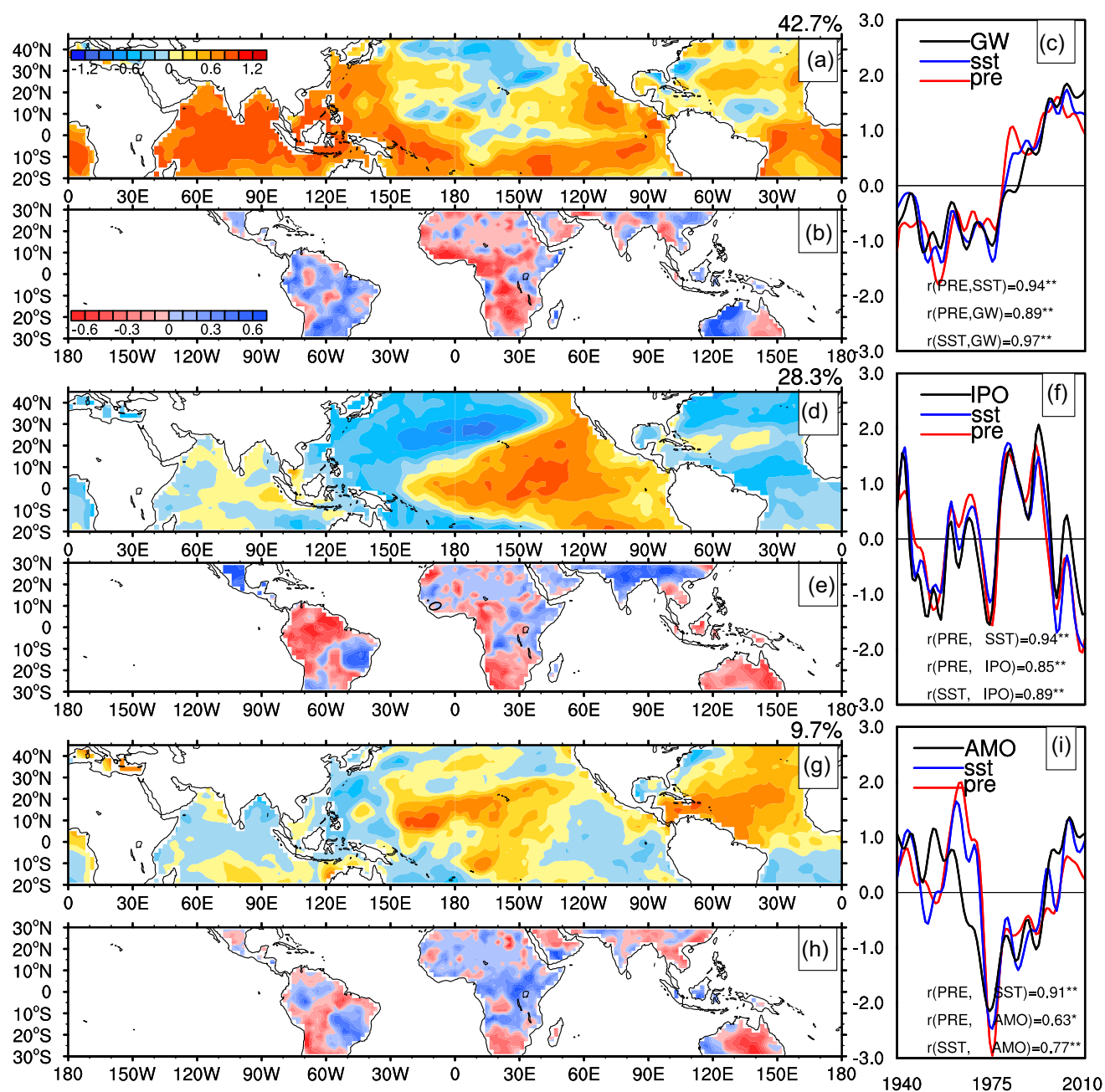


Fig. 2 Same as Fig. 1, but for the precipitation from CRU in DJF. The variances of the first three SVD modes are 42.7%, 28.3%, 9.7%, respectively

so-obtained series may be contaminated by decadal/interdecadal oscillations, we further apply the ensemble empirical mode decomposition (EEMD) (Wu and Huang 2009) to remove the decadal/multi-decadal variability, and keep the noticeable non-linear upward trend as the GW index; see Fig. 3. [EEMD is an adaptive time-space analysis method suitable for processing series that are non-stationary and non-linear and separate scales naturally without any a priori subjective criterion selection as in the intermittence test for the original EMD algorithm (Wu and Huang 2009)].

The AMO and IPO monthly time series are provided by NOAA Earth System Research Laboratory's Physical Sciences Division (PSD) (<https://www.esrl.noaa.gov/psd/data/climateindices/list/>). The AMO series is estimated as the detrended-area-weighted SST averaged over the North Atlantic (0–70° N). The IPO time series is taken as the difference between the SST anomalies (SSTA) averaged over the central equatorial Pacific and that averaged over the Northwest and Southwest Pacific.

Fig. 3 Time series of the 9-year low-passed AMO (blue line), IPO (black line) and GW (red line) indices from 1394–2015. EEMD has been applied to the domain averaged SST over (45° S–60° N); the trend is used as the GW index

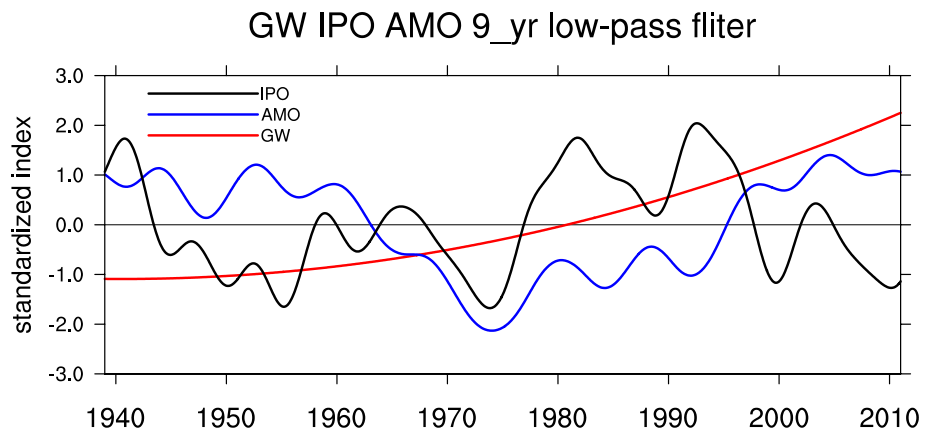


Table 1 Correlation coefficients between GW, AMO, and IPO

	GW	AMO	IPO
GW	1	0.13	0.07
AMO	0.13	1	-0.18
IPO	0.07	-0.18	1

2.2 Methods

2.2.1 Singular value decomposition

The singular value decomposition (SVD) analysis (Bretherton et al. 1992) is used to identify the dominant precipitation patterns and their coupling to the SST. The tropical land rainfall over (30° S–30° N) is taken as the left field and the SST over (20° S–45° N) as the right field. The reason for choosing the precipitation over tropical region rather than that over global region is that the variance contributions of dominant ocean modes differ from region to region; we can't extract the dominant ocean modes if we use the global precipitation. For example, we have applied SVD analysis to the dataset of precipitation over the North America and the SST dataset over (20° S–45° N). The resulting dominant ocean modes are AMO in JJA and IPO in DJF. When precipitation data is changed to that over East Asia, the first dominant mode becomes GW, rather than AMO or IPO. Anyway, the dominant ocean modes are no more than GW, AMO and IPO. For the above reason and due to the large land area over tropics, the tropical land rainfall over (30° S–30° N) is used as left field for the SVD analysis.

2.2.2 Multivariate linear regression

Multivariate linear regression method (Grömping 2006) is applied to evaluate the relative contributions of GW, AMO and IPO to the global land precipitation variation. We regress the annual mean precipitation onto GW, AMO and IPO indices. By Table 1, the GW, AMO and IPO indices can be considered

as independent variables—The degrees of freedom determined by the autocorrelation (Dawdy and Matalas 2020) and correlation coefficients between them suggests that they are statistically insignificant by the Student's *t* test. The multivariate linear regression model is given as:

$$PRE_i = \beta_0 + \beta_1 GW_i + \beta_2 \cdot AMO_i + \beta_3 \cdot IPO_i + e_i \quad (1)$$

where *i* signifies time step, β_0 , β_1 and β_2 are regression coefficients, e_i is the residual part which cannot be explained by the model, which here we assume to follow a Gaussian distribution around zero. The proportion that can be explained by the three indices is calculated as:

$$R^2 = \frac{Model_Var}{Total_Var} = \frac{\sum_{i=1}^t (\widehat{PRE}_i - \overline{PRE})^2}{\sum_{i=1}^t (PRE_i - \overline{PRE})^2} \quad (2)$$

where,

$$\widehat{PRE}_i = \hat{\beta}_0 + \hat{\beta}_1 \cdot GW_i + \hat{\beta}_2 \cdot AMO_i + \hat{\beta}_3 \cdot IPO_i \quad (3)$$

In Eqs. (1) and (2), the overbar denotes the climatological mean value, and the caret denotes the value estimated from the linear regression model. Suppose *Q* is the residual variance of e_i in Eq. (1) which cannot be explained by GW, AMO and IPO. Then we can get a new multivariate regression formulation and new residual variance Q'_{GW} if we take away one independent variable, for example GW. Obviously, the less the independent variable considered, the larger the residual variance becomes. We then obtain the variance contribution from GW:

$$Q_{GW} = Q'_{GW} - Q. \quad (4)$$

Likewise, the contributions from AMO and IPO are also obtained:

$$Q_{AMO} = Q'_{AMO} - Q \quad (5)$$

$$Q_{IPO} = Q'_{IPO} - Q \quad (6)$$

We hence can calculate the proportion of variance explained by GW, AMO and IPO, using the following formulas:

$$R_{GW} = \frac{Q_{GW}}{Q_{GW} + Q_{AMO} + Q_{IPO}} \quad (7)$$

$$R_{AMO} = \frac{Q_{AMO}}{Q_{GW} + Q_{AMO} + Q_{IPO}} \quad (8)$$

$$R_{IPO} = \frac{Q_{IPO}}{Q_{GW} + Q_{AMO} + Q_{IPO}} \quad (9)$$

2.2.3 Information flow

Usually, we use time-lagged correlation analysis to identify the causality between two time series. However, it is well known that correlation does not carry the needed directedness or asymmetry and hence does not necessarily imply causality. During the past decade, it has been realized that causality is inherently rooted in information flow, a real physical notion which can be rigorously formulated from first principles (Liang 2016). This formalism has been well validated with benchmark dynamical system problems. Moreover, under some assumptions, its maximum likelihood estimator is shown to be very concise in form (Liang 2014). This formula has been applied successfully to the investigation of many real-world problems in a variety of disciplines such as neuroscience, finance, atmosphere-ocean science, etc. In climate science, it has been used to reveal to us a mutual causal relation between El Nino and Indian Ocean Dipole (Liang 2014), a clear one-way causality between CO₂ and the global temperature (Stips et al. 2016), so on so forth. In this study, we adopt it to cross-validate the results with the above methods.

Consider a two-dimensional dynamical system (with components standing for the time series to be studied):

$$\frac{dX_1}{dt} = F_1(X_1, X_2, t) + b_{11}\dot{W}_1 + b_{12}\dot{W}_2 \quad (10)$$

$$\frac{dX_2}{dt} = F_2(X_1, X_2, t) + b_{21}\dot{W}_1 + b_{22}\dot{W}_2 \quad (11)$$

where W_1 and W_2 are white noises, F_1, F_2 are differentiable functions of their variables, Liang (2014) proved that the information flow from X_2 to X_1 , written $T_{2 \rightarrow 1}$, is

$$T_{2 \rightarrow 1} = -E \left[\frac{1}{\rho_1} \frac{\partial(F_1 \rho_1)}{\partial x_1} \right] + \frac{1}{2} E \left[\frac{1}{\rho_1} \frac{\partial^2 (b_{11}^2 + b_{12}^2) \rho_1}{\partial x_1^2} \right] \quad (12)$$

where E represents mathematical expectation, $\rho_1 = \rho_1(x_1)$ is the marginal probability density function of X_1 . Ideally, when $T_{2 \rightarrow 1} = 0$, X_2 is not causal to X_1 ; otherwise, it is causal. In real applications, statistical significance should be tested. The units for $T_{2 \rightarrow 1}$ is nats per unit time.

The above formula is difficult to apply. Later, Liang (2014) proved that, under a linear assumption, its maximum likelihood is remarkably simple:

$$T_{2 \rightarrow 1} = \frac{C_{11}C_{12}C_{2,d1} - C_{12}^2C_{1,d1}}{C_{11}^2C_{22} - C_{11}C_{12}^2} \quad (13)$$

where $T_{2 \rightarrow 1}$ is now understood as the maximum likelihood estimator, C_{ij} is the covariance between X_i and X_j , and $C_{i,dj}$ is the covariance between X_i and a derived series using Euler forward differencing scheme:

$$\dot{X}_j = \frac{X_{j,n+1} - X_{j,n}}{\Delta t} \quad (14)$$

More details are referred to Liang (2014). By applying Eq. (12), we can obtain, in a quantitative sense, the causalities from GW, AMO and IPO to the precipitation at each grid, and hence their respective impacts. Significant tests (Liang 2014) will also be conducted.

2.2.4 AGCM experiments

To further substantiate the results, a set of SST sensitivity experiments will also be performed using the atmospheric general circulation model (AGCM) ECHAM version 4.6. The model was developed at the Max Planck Institute for Meteorology (MPI; Roeckner et al. 1996) and evolved originally from the spectral weather prediction model of the European Centre for Medium Range Weather Forecasts (ECMWF). It is a spectral model with a triangular truncation at the wavenumbers 42 (T42) and 106 (T106). In our experiments, we choose the T42 resolution (roughly equivalent to 2.8°·2.8° in latitude and longitude) and 19 vertical levels. For each experiment, it is integrated for 30 years, and outputs the results of the last 20 years for analysis.

3 Results

3.1 Dominant SST modes contributing to the trend/decadal precipitation variability

To explore the spatial distributions of coupling between the decadal variations in precipitation and SST, an SVD analysis is performed for the tropical land precipitation (30° N–30° S) and SST (45° N–20° S). As a pretreatment, we first remove the seasonal cycles and high-frequency variations

with a 9-year Lanczos low-pass filter. Considering that JJA and DJF mean precipitation patterns are different, the boreal summer and boreal winter cases are distinguished.

The first three coupled modes and the related time series resulting from the SVD analysis are displayed in Figs. 1a–i and 2a–i. The variances they possess are, respectively, 48.7%, 24.3% and 8.5% for JJA, and 42.7%, 28.3% and 9.7% for DJF.

The first SST mode reveals a unified SST warming both during JJA and DJF (Figs. 1a and 2a) except in the subtropical central Pacific. The warming rates in the Indian Ocean, tropical Pacific and tropical South Atlantic are larger than other regions. In the subtropical central Pacific, the SST variation appears as a cooling trend, which somehow differs from the consistent global scale SST warming found in previous studies (Cane 1997; Hansen et al. 2006; Xie et al. 2010; Mohino et al. 2011; Gu and Adler 2015). It implies that this mode is probably mixed with decadal/interdecadal oscillations which the SVD analysis cannot have them separated. The principal components (PC1s) of SST and precipitation are generally consistent with the trend of observed global mean SST (45° S– 60° N) in JJA (Fig. 1c); their time series show an increasing trend over the whole period. A weak decreasing trend is visible from 1943 to 1970, which may be partially related to changes in global mean temperature due to or the anthropogenic aerosols during that period (e.g., Wilcox et al. 2013), or may be due to the residual decadal/interdecadal SST signals (Dong and McPhaden 2017a, 2017b). A general reduction in precipitation is seen over the tropical areas in its first mode, as the SST increases (Fig. 1b), consistent with previous studies (e.g. Zhang et al. 2007; Gu and Adler 2015). An enhanced precipitation area appears in the Gulf of Guinea, as the one shown in Mohino et al. (2011). Over north Australia, the rainfall shows a large drying trend.

For the second SVD mode during JJA, the spatial patterns and related PCs are shown in Fig. 1d–f. The SST pattern is characterized by warm anomalies in the entire Northern Atlantic and most of the Northern Pacific, implying a teleconnection between the two ocean basins. The time series of SST and precipitation show a consistent change with the AMO index after 1950, though some discrepancies exist before 1950s. The correlation coefficient between the SST time series and AMO index is up to 0.78. That is to say, the second SST mode is essentially from AMO. During the positive phase of AMO, the AMO-related rainfall variability (Fig. 1e) over Sahel shows a robust above-average rainfall, in opposition to the pattern associated with GW (Fig. 1b). In the next section, we will investigate the relative contributions of GW, AMO and IPO to the rainfall over Africa, and that over other regions in next section. Over South America, negative anomalies are found, except for a small area of northwestern South America. The precipitation

over Australia is generally below average during the positive AMO phase.

The third mode during JJA, including its spatial patterns of SST and precipitation and their related PCs, are shown in Fig. 1g–i. The horseshoe SSTA pattern as shown in Pacific is similar to the IPO signal; the correlation coefficient between them is up to 0.83. The IPO index is also highly correlated to the time series of precipitation, with a coefficient being 0.65. Notice that IPO is the third contributor to the decadal/interdecadal variability of the JJA tropical precipitation. Its contribution to the variance is only 8.5%. The IPO-related rainfall variability shows a rather weak positive anomaly over almost entire Africa except Congo Basin. In South America, positive rainfall anomalies are observed in eastern Brazilian plateau.

In the DJF season (Fig. 2), the GW (Fig. 2a–c) is still the first dominant mode with the biggest variance contribution (42.6%). The precipitation related to GW over Australia is characterized by an east–west dipole pattern, in a way as the eastern Australia is getting wet and the western Australia getting dry. With GW, Africa also becomes dry in DJF, as in JJA. In DJF, IPO is the second contributor to the decadal/interdecadal variability of tropical precipitation, with a variance of 28.3% (Fig. 2d, f). The correlation coefficient of its index with the SST series of SST is 0.89, and that with the precipitation series is also as high as 0.85 (Fig. 2f). During the positive IPO phase, the conspicuous dry anomalies are seen in the southern Africa, northern Australia and northwestern South America. Wet anomalies are seen in southern Asia except Indochina Peninsula (Fig. 2e). In this season, AMO is the third contributor to the decadal/interdecadal variability of tropical precipitation, only with 9.7% of the variance (Fig. 2g, i). The correlation coefficient between the time series of SST (precipitation) and the AMO index is 0.77 (0.63). During the positive AMO phase, the precipitation increases in Africa, decreases in Central Australia (Fig. 2h).

3.2 Regression map

The above results demonstrated that GW, AMO and IPO are three dominant modes contributing to the trend/interdecadal variation of land precipitation, especially over the tropical land areas. In this section, the effects on the trend/interdecadal variation of the land precipitation at high latitudes are investigated. The regression maps of JJA and DJF precipitations against GW, AMO and IPO indices are respectively constructed and compared to the SVD results.

In order to isolate the GW effect from the long time series of the global mean SST, before regression the high frequency signals are removed using the EEMD method. A 9-year Lanczos low-pass filter is applied to the AMO, IPO time series and the precipitation signals to remove the

interannual variations. The resulting three series are displayed in Fig. 5.

Figure 4a–f show the regressed JJA and DJF precipitations against the GW, AMO and IPO indices. Over the tropical land, the JJA and DJF precipitations regressed onto the GW index (Fig. 4a, b) highly resembles that from the SVD analysis, with pattern correlation coefficient of 0.67 for JJA and 0.70 for DJF. In JJA, a dry trend is found over the tropical land, northern China, Mongolia, eastern Russia, the south of Himalayas and Gran Chaco in South America, and wet trend found in Canada, southeastern and northwestern China, and Scandinavia. In DJF, a wet trend is seen in western Australia, South America and Europe, and a dry trend identified in the southern Africa, western Canada and eastern Russia.

The regressed JJA and DJF precipitations against AMO (Fig. 4c, d) are consistent with the second SVD spatial

pattern of precipitation over the tropical regions, with pattern correlation coefficient of 0.62 for JJA and 0.54 for DJF. Besides the robust increased JJA rainfall over Sahel and reduced JJA rainfall over Guinea Gulf during the AMO positive phase (Zhang and Delworth 2006; Mohino et al. 2011), wet anomalies are also found in the north of Russia, southeastern Asia, Alaska and the western coast of Europe. During the DJF AMO positive phase, significant dry anomalies are seen in the middle of Australia and wet anomalies around Lake Baikal.

The regressed JJA and DJF precipitation fields against IPO (Fig. 4e, f) are also consistent with their corresponding SVD patterns over the tropical regions except west Africa where dry anomalies are evident in JJA during the positive IPO phase (Fig. 4e). Besides that, dry anomalies are found over central Russia, and wet anomalies along the belt from the eastern European plain to the northeastern

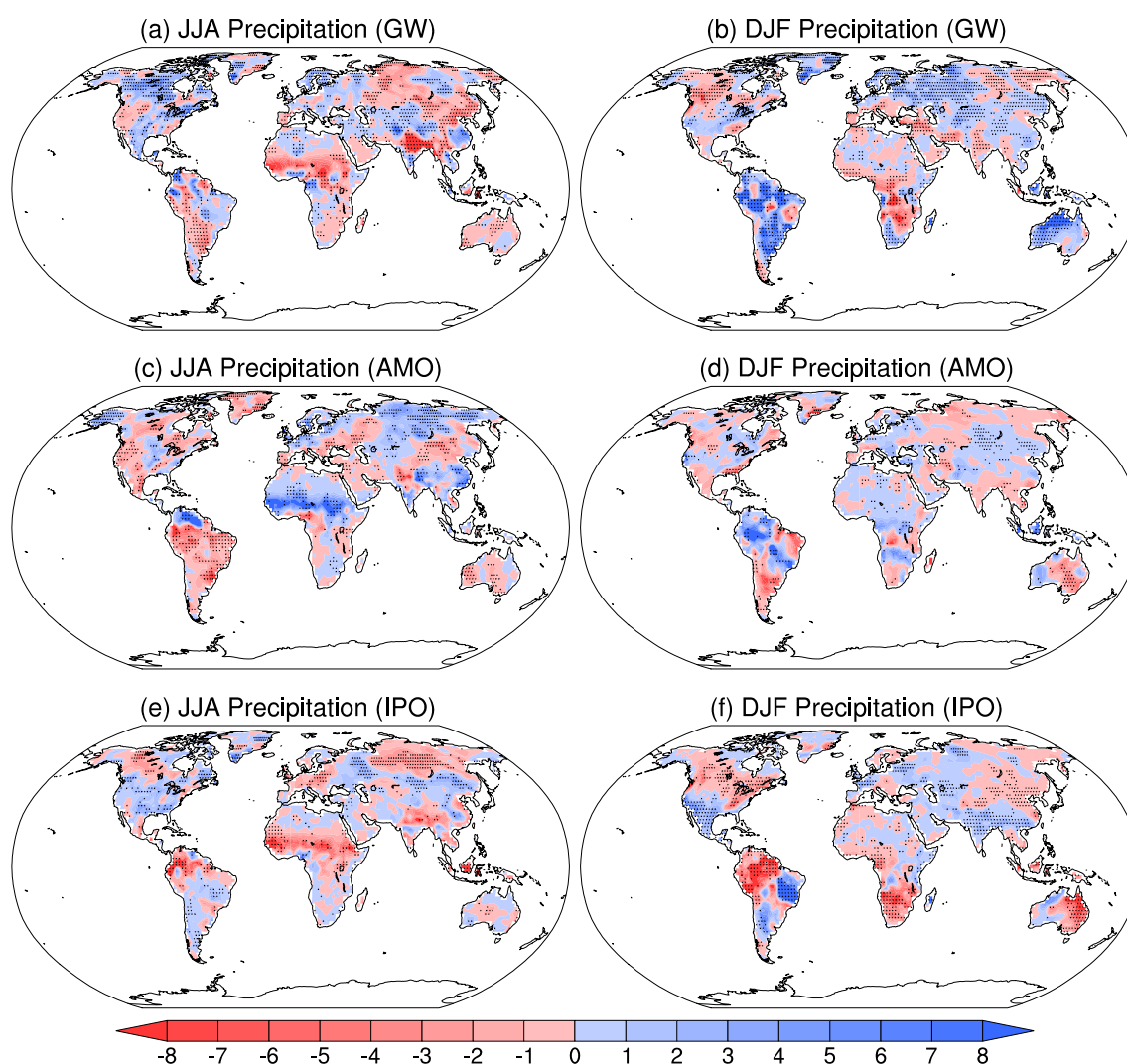


Fig. 4 Regressed land precipitation from CRU (mm mon^{-1}) in JJA (left column) and DJF seasons (right column) onto to the normalized indices of GW (a, b), AMO (c, d) and IPO (e, f). The areas with dots are statistically significant at the 10% level

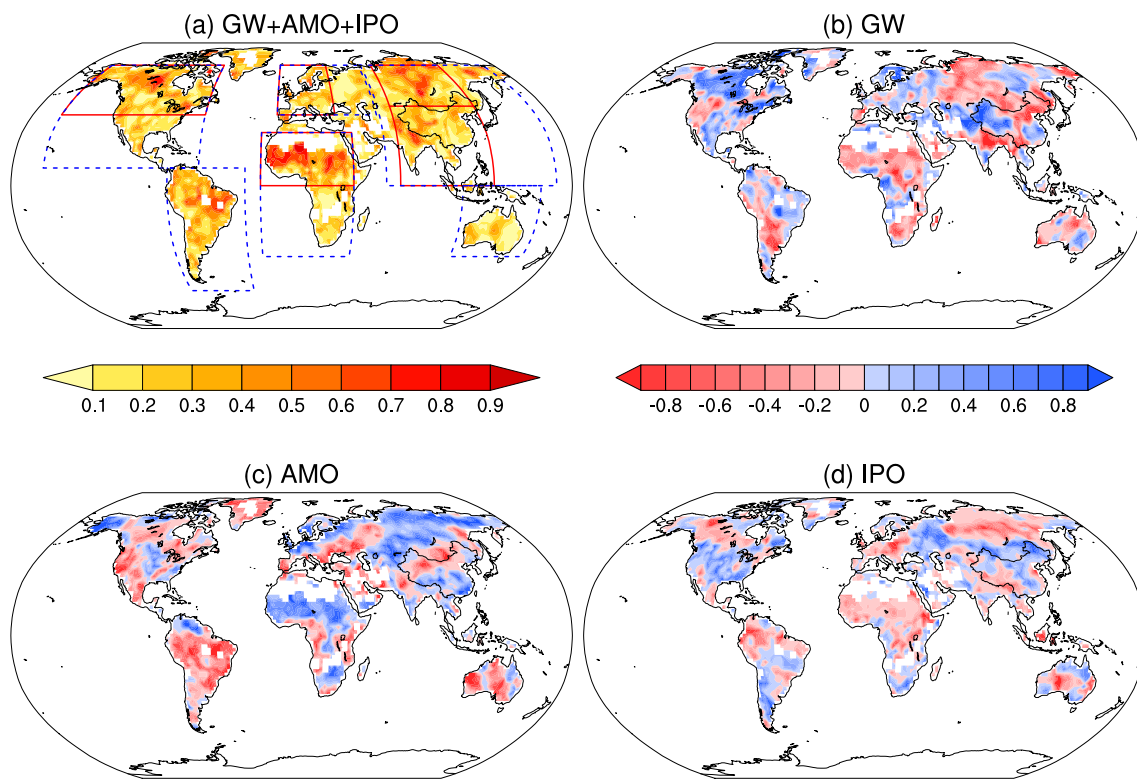


Fig. 5 **a** Total variance contributions of GW, AMO and IPO to the low-frequency variability of land precipitation from CRU in JJA of 1934–2015, and relative contributions of **b** GW, **c** AMO and **d** IPO.

The negative areas signify the negative regressed precipitation with the variance fractions. The boxes in **a** are the domains specified to calculate the domain-averaged relative contributions in Fig. 6

China (Fig. 4e). The pattern correlation coefficient is 0.47 for JJA, and 0.72 for DJF. IPO has a more significant impact on precipitation during DJF (Fig. 4f). Seesaw structures of precipitation anomalies are observed in the northeastern and southwestern North America, with wet anomalies over the southwestern United States. Wet anomalies are also found over the South Asia monsoon region, Brazilian plateau, and dry anomalies over Canada, Amazon Basin, southern Africa and East Australia during the DJF season of the positive IPO phase, in agreement with previous studies Meehl and Hu 2006; Meehl et al. 2013; Dai 2013; Reason and Rouault 2002; Krishnan and Sugi 2003; Verdon et al. 2004; Henley et al. 2013; Dong and Dai 2015).

The above analyses confirm that GW, AMO and IPO are the three dominant modes modulating the trend/interdecadal variation of land precipitation. In the following, we give an evaluation of their importance relative to each other.

3.3 Relative contributions of GW, AMO and IPO

The above results show that the low-frequency variability of land precipitation during 1934–2015 can be interpreted as the joint effect of GW, AMO and IPO. In this section their relative contributions are investigated. The total variance

contribution to the low-frequency land precipitation variability is obtained via multivariate regression (Eq. 1). Shown in Fig. 5b–d are the respective percentages. It should be noted that their sum equals to 1, rather than the total variance contribution explained by the linear regression model.

As shown in Figs. 5a and 6, not all the low-frequency variability of land precipitation can be explained by the three modes. On average, they can make about 30% of the trend/interdecadal variability. Locally, the amount can be as high as more than 40% for JJA precipitation over Canadian Shield in North America, Brazil Plateau in South America, Sahel, Siberia, southern Himalayas, and for the DJF precipitation over southwestern US, Argentina, west Siberia Plain and East Australia. The region dependence is clearly seen in Fig. 6, for the JJA precipitation, the three can explain 43% of that over northern Africa, but account for only 19% of that over Australia.

3.3.1 The JJA season

Consider the JJA season first (Figs. 5 and 6). Over Africa, especially over the northern Africa, AMO plays a dominant role on the precipitation variation, contributing 44% of the 43% variance. GW and IPO contribute the

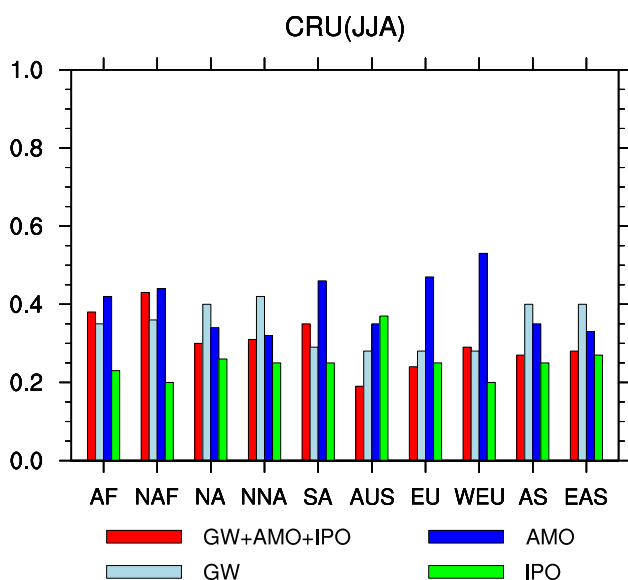


Fig. 6 Domain-averaged total variance contributions of GW, AMO and IPO to the low-frequency variability of JJA land precipitation from GPCC, and the relative contributions of GW, AMO and IPO, respectively. Domains are: Africa (AF: 20° W–40° E, 40° S–30° N), northern Africa (NAF: 20° W–40° E, 0–30° N), North America (NA: 160° W–60° W, 10° N–70° N), northern North America (NNA: 160° W–60° W, 40° N–70° N), South America (SA: 80° W–30° W, 60° S–10° N), Australia (AS: 110° E–160° E, 40° S–0), Europe (EU: 10° W–60° E, 40° N–70° N), West Europe (WEU: 10° W–30° E, 40° N–70° N), Asia (AS: 60° E–180° E, 0–70° N) East Asia (EAS: 70° E–130° E, 0–70° N)

remaining 36% and 20%, respectively. Over the northern North America, GW dominates, contributing 40% of the explained 30% variance. This region gets wet with GW. Secondary to GW, AMO and IPO make the remaining 34% and 26%, respectively. Over South America, AMO's role is dominant, accounting for 46% of the explained 35% variance. More specifically, negative precipitation anomalies are observed during AMO's positive phase. GW and IPO make the remaining 29% and 25%, respectively. Over Europe, especially over West Europe, AMO also plays a dominant role, making 53% of the 29% variance, and reduction in rainfall is related to the positive phase of AMO. The contributions of GW and IPO are 28% and 20%, respectively. Over Asia, GW dominates, contributing 40% of the explained variance (27%). This region becomes dry with GW except northwestern China. Secondary to GW, AMO and IPO contribute 35% and 25%, respectively. Over Australia, it is IPO that plays a dominant role, accounting for 37% of the explained variance (19%). Secondary to IPO, AMO and GW contribute 35% and 28%, respectively.

3.3.2 The DJF season

The results for the DJF season are shown in Figs. 7 and 8. In DJF, GW dominates the precipitation variability in most areas except for southern North America, where IPO is the dominant mode. Over Africa, GW contributes 42% of the 26% variance. Second to it is IPO, which makes 33% of the variance. This region becomes dry with GW and in positive IPO phase. Over North America, GW accounts for 41% of the explained 27% variance, taking the leading role. It is followed by IPO, which contributes 34% of the variance, and by AMO, which makes the remaining 25%. Over southern North America, IPO dominates, making 55% of the explained 33% variance. The region is wet during the positive phase of IPO. Over Europe, GW is dominant, making 52% of the 27% variance. It gets wet over Europe with GW, especially over West Europe. AMO and IPO contribute equivalently, both being 24%. Over Asia, GW accounts for 45% of the explained 33% variance. AMO and IPO also have the same contribution (28%). Over Australia, GW's contribution totals 39% of the 30% variance. Australia, especially West Australia is getting wet with GW. The role of IPO is secondary, accounting for 34% of the variance, and AMO comes next, with a fraction contribution of 27%.

Figure 9 shows the zonal averages of the percent variances of GW, AMO and IPO to the JJA and DJF land precipitations from CRU. In JJA, the contributions of GW, AMO and IPO to the land precipitation are of the same order in the thin latitude bands: 10° S–10° N, 50° N–60° N and 40° S–50° S. Outside GW and AMO dominate. In DJF, the AMO contribution is smallest from 40° S to 50° N. IPO plays a dominant role between the latitudes 20° S and 40° N. Beyond 20° S–40° N, GW's role is most important.

3.4 Causality between ocean modes and land precipitation

To cross-validate the above results, a recently developed causality analysis is applied to re-investigate the impacts of GW, AMO and IPO on the land precipitation variability. This causality analysis, which is based on information flow, a real physical notion which has been under development in physics for more than 30 years, is distinctly different from the other causal inference techniques in that it is rigorously derived from first principles in physics, and it is quantitative hence capable of giving us patio temporal structures. Besides, it is a physical notion, not a statistical notion. Basically, when a computed rate of information flow from one event A to another event B is nonzero, then A is causal to B, and the magnitude tells the size of causality. In real problems, of course, significance test should be performed. It should be noted that the causality from A to B has nothing to

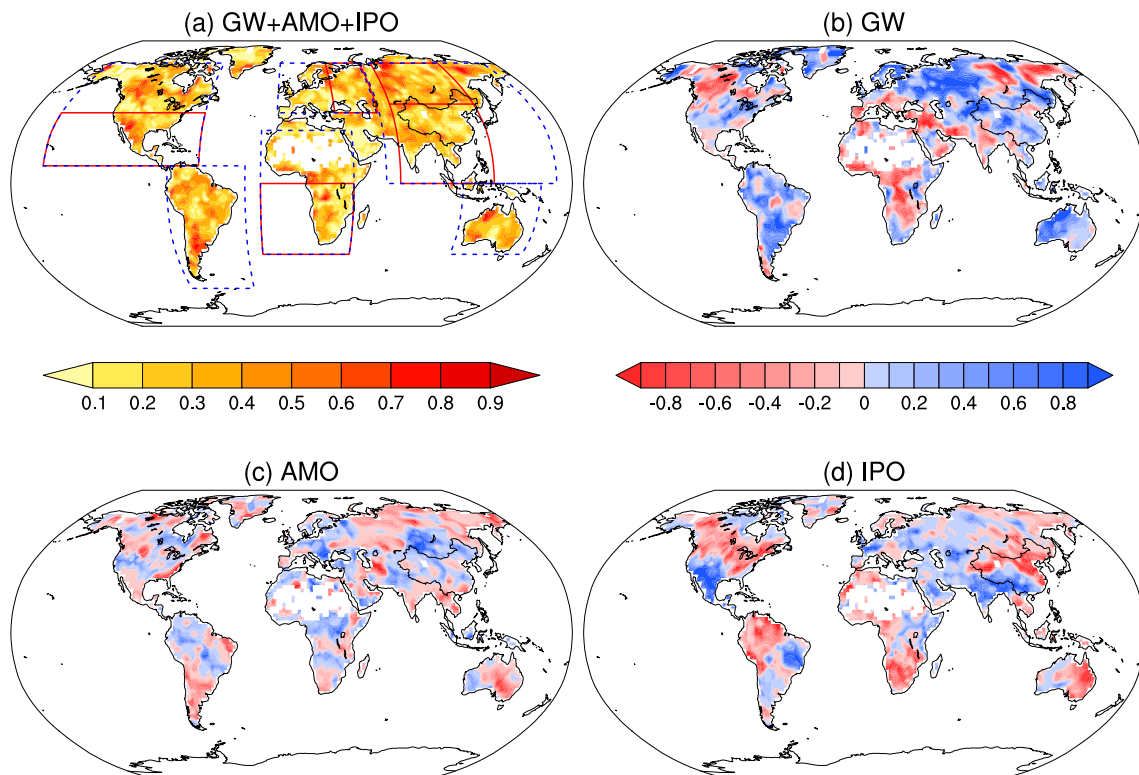


Fig. 7 Same as Fig. 5, but for the precipitation from CRU in DJF. The boxes in a are the domains specified to calculate the domain-averaged relative contributions in Fig. 8

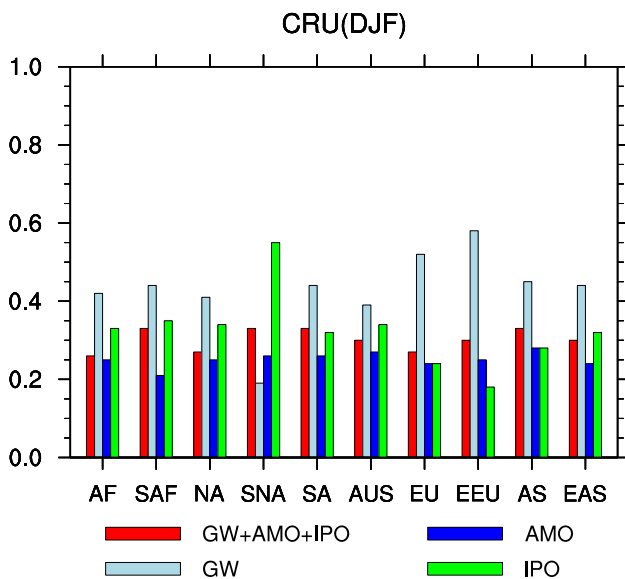


Fig. 8 Same as Fig. 6, but for the precipitation from CRU in DJF. Domains which are not defined in Fig. 6 are: Southern Africa (SAF: 20° W–40° E, 40° S–0), Southern North America (SNA: 160° W–60° W, 10° N–40° N), East Europe (EEU: 30° E–60° E, 40° N–70° N)

do with that from B to A. This is completely different from correlation analysis.

Figure 10a shows the information flow between GW and the land precipitation from the CRU dataset. It is computed using Eq. (10) between the GW index and the CRU rainfall time series at each grid point. Clearly, GW is significantly causal to precipitation over many regions, and the causality pattern (Fig. 10a) is similar to the fraction of variance explained by GW (Figs. 7b and 8b) over Greenland, Scandinavia, Canadian Shield, the south of Great Lakes in North America, southern South America, Africa, the central and northern Eurasian and western Australia. In contrast, this causality is not significant over the eastern Eurasian. This is different from the results in Fig. 7b.

The information flow from AMO to precipitation is depicted in Fig. 10b. Obviously, over Sahel, Siberia, southern United States, northeastern South America and central Australia, the causality is significant, which means precipitation variation over these regions can be explained by the AMO. This is consistent with the fractions of variance contributions (Figs. 7c and 8c).

Figure 10c displays the information flow from IPO to precipitation. Significant causality has been detected around southwestern United States, northeastern and southern South America, southern Africa, Kazakhstan and Uzbekistan, most

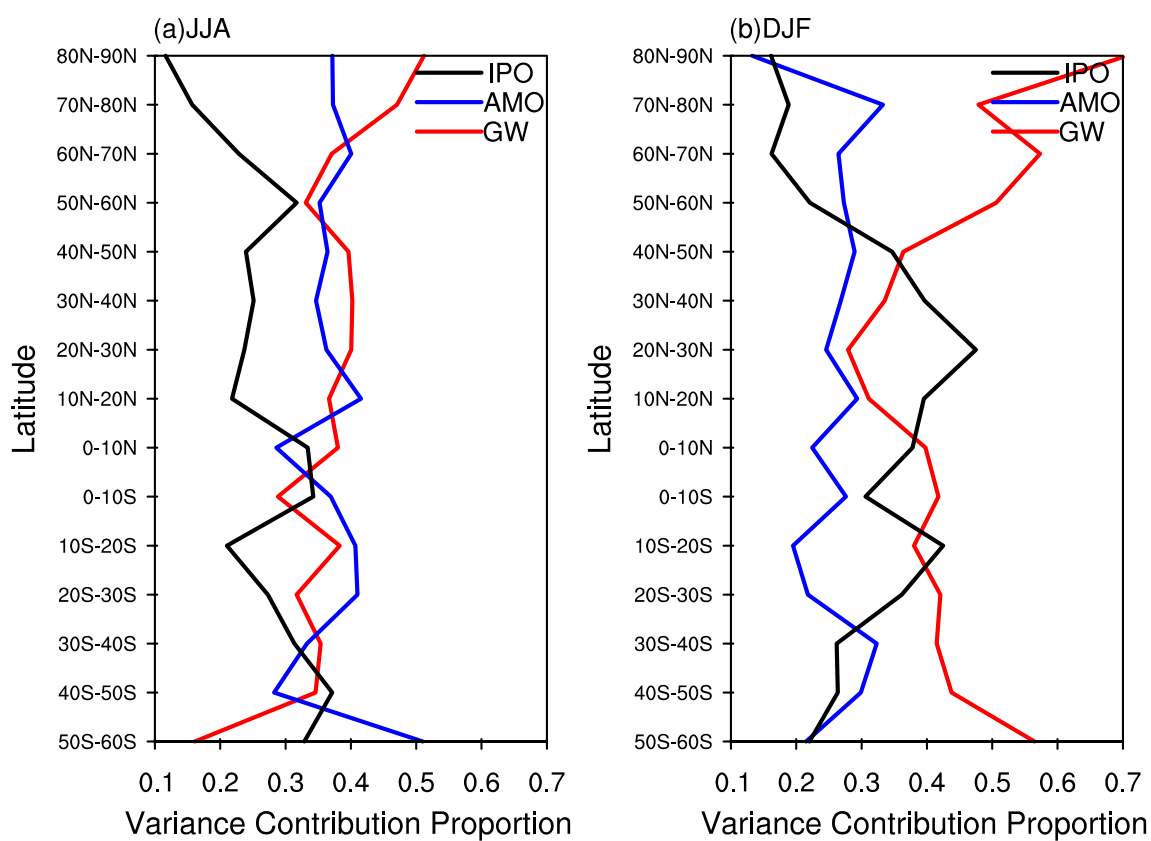


Fig. 9 Zonal averaged relative contributions of GW (red line), AMO (blue line) and IPO (black line) to **a** the land precipitation from CRU in JJA and **b** the land precipitation in DJF

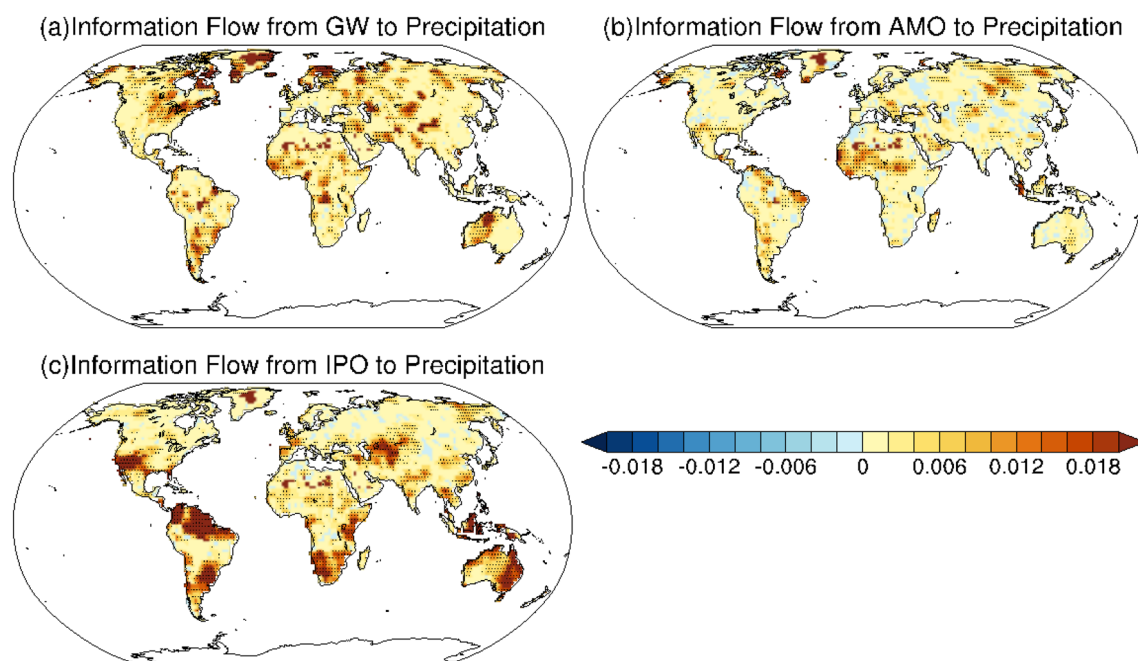


Fig. 10 Information flow from **a** GW, **b** AMO and **c** IPO to the land precipitation from CRU in 1934–2015. The areas with dots are statistically significant at the 10% level

area of Australia except Great Victoria Dessert, and south-eastern and northern China. This causal pattern is similar to the fraction distribution of variance contribution as shown in Fig. 8d.

Obviously, the causal relations are mostly consistent with the SVD and regression results, which are henceforth cross-validated.

3.5 Numerical experiments

To further substantiate the inferred impacts of AMO and IPO on the land precipitation variation, five sets of numerical experiments are conducted using the ECHAM version 4.6. Table 2 is a summary of these experiments.

The control run (CTL) of the experiments is driven by the observed climatological monthly SST from 1934 to 2015. We need to take a look at the SST anomalies related to AMO and IPO.

Figure 11 a, b show the global SSTs regressed onto the 1935–2015 AMO and IPO indices (Fig. 3), which correspond to the positive phases of the AMO and IPO signals, respectively. Before regression, the high-frequency and seasonal cycle signals have been removed from the monthly series with a 9-year Lanczos low-pass filter. As shown in Fig. 11a, the positive AMO phase is associated with the basin-wide warmer SST over the North Atlantic Ocean and cooler SST over the South Atlantic. There are also positive loadings over the tropical Indian Ocean and Pacific. Mohino et al. (2011) suggested that the positive phase of the AMO is associated with cooler SST over the tropical Indian Ocean. However, they failed to obtain the increased Sahelian rainfall with the forcing of the positive SSTA over North Atlantic and the negative SSTA over tropical Indian Ocean. Zhang and Delworth (2006) achieved the perfect wet/drought pattern over Sahel with a hybrid coupled model. In our study, as will be seen soon, the wet (drought) pattern over Sahel can't be forced by

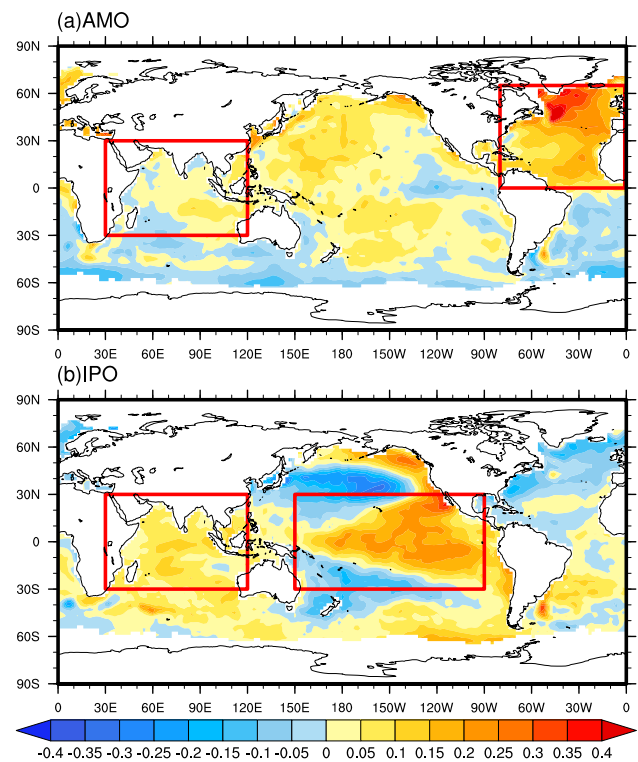


Fig. 11 Regressed SST ($^{\circ}\text{C}$) onto **a** the AMO and **b** IPO indices. The rectangular boxes are the specified SSTA domains

the only the positive (negative) SSTA over North Atlantic in the absence of the tropical Indian Ocean SSTA. As shown in Fig. 12b, the IPO-associated SST pattern shows the familiar ‘horse shoe’ pattern over the Pacific, with the positive anomalies over the tropical central eastern Pacific and the negative anomalies over the North Pacific. There is also a positive loading over the Indian Ocean, which agrees with that in many previous studies (e.g. Cole et al. 2000; Han et al. 2014; Dong et al. 2016; Dong and McPhaden 2017a, b), where the decadal/interdecadal

Table 2 Summary of the ECHAM4 model experiments

Experiments name	Area of anomalous SSTs
CTL run	Observed climatological monthly SST
AMO experiments	
Warm AMO_NA run	Add or subtract the positive SST anomalies over the North Atlantic
Cold AMO_NA run	
Warm AMO_NAI run	Add or subtract positive SST anomalies over the North Atlantic and the Indian Ocean
Cold AMO_NAI run	
IPO experiments	
Warm IPO_TP run	Add or subtract the positive SST anomalies over the tropical Pacific
Cold IPO_TP run	
Warm IPO_TPI run	Add or subtract the positive SST anomalies over the tropical Pacific and the Indian Ocean
Cold IPO_TPI run	

Climate Precipitation and 850hPa UV

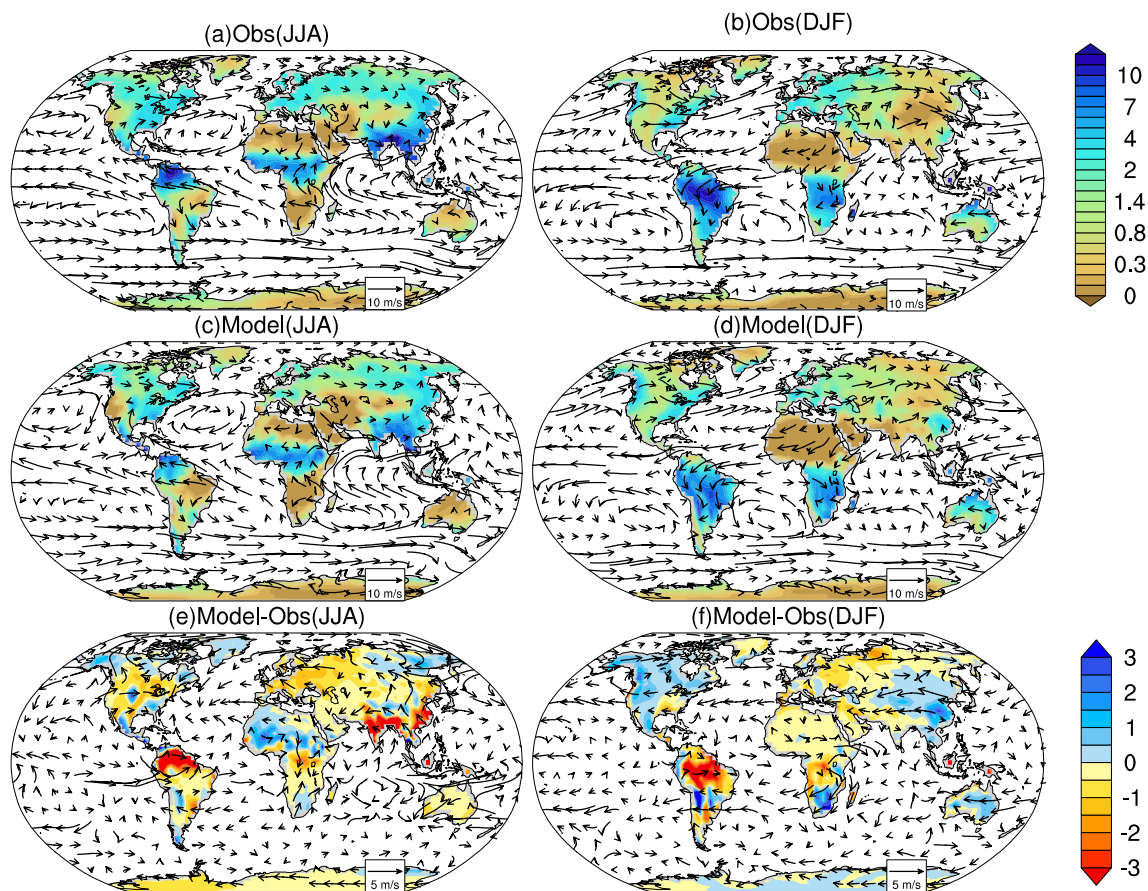


Fig. 12 Precipitation and 850-hPa horizontal winds for observation **a, b** and the CTL run **c, d** and the differences between them

variability of Indian Ocean is observed to be highly related to IPO. This suggests that the SST over the tropical Indian Ocean is partially co-varying with IPO or AMO.

As said above, the control run (CTL) is forced with the observed 1934–2015 climatological monthly SST. For the other four sensitivity experiments (Table 2), the SST defined as positive anomalies in different domains (Fig. 11) is added to the observed climatology. They are, specifically,

- Run 1 (hereafter warm AMO_NT run): positive SST anomalies over the domain of the North Atlantic (0° – 65° N, 80° W– 0°), as shown in Fig. 11a, are superimposed to the climatology;
- Run 2 (hereafter warm AMO_NTI run): positive SST anomalies over both domains of the North Atlantic (0° – 65° N, 80° W– 0°) and the tropical Indian Ocean (30° S– 30° N, 30° E– 100° E) (Fig. 11a) are added to the climatology;
- Run 3 (hereafter warm IPO_TP run): positive SST anomalies over the tropical Pacific (30° S– 30° N, 150° E– 90° W) (Fig. 11b) are superimposed to the climatology;

- Run 4 (hereafter warm IPO_TPI run): positive SST anomalies over both the tropical Pacific (30° S– 30° N, 150° E– 90° W) and the tropical Indian Ocean (30° S– 30° N, 30° E– 100° E) (Fig. 11b) are superimposed to the climatology.

The cold experiments are conducted with the positive SSTA in specified domains subtracted from the observed climatological monthly SST. The model is integrated for 30 years in each experiment and the results of the last 20 years are analyzed below.

Figure 12 shows the mean land precipitation and the 850-hPa wind from the observation (Fig. 12a, b) and control run (Fig. 12c, d) during the JJA and DJF seasons, respectively. As can be seen, the common features of the anticyclones over the north Pacific and the North Atlantic and the cross equatorial flow over the Indian Ocean during JJA are well reproduced. Discrepancies do exist (Fig. 12e, f), of course. For example, the monsoon trough in the western Pacific and southerly along the East Asian coast are modeled weak in JJA, causing insufficient JJA rainfall over East Asia, and the

modeled rainfall in southern South Africa is too weak both in JJA and DJF.

Figure 13 shows the different precipitation and 850-hPa horizontal winds in JJA and DJF in the warm AMO_NA run and cold AMO_NA run, those in the warm AMO_NAI run and cold AMO_NAI run, and the difference between them. During the JJA of the positive AMO phase, positive precipitation anomalies over Sahel are only reproduced in the AMO_NAI run (Fig. 13c), not in the AMO_NA run. The AMO_NAI experiment also captures the positive precipitation anomalies over South China and the negative precipitation anomalies over northeastern North America, Mexica and central South America (Fig. 13c, e), agreeing with the regression results in Fig. 4c. The circulation anomalies over the North Atlantic are characterized by cyclonic anomalies at 850 hPa. The anomalous cyclone brings cold dry air to America, and warm moist air to the northern

Africa during JJA, causing the dry and wet conditions in these areas. Meanwhile, anomalous westerly winds from the ocean enhances precipitation in East Asia. During the DJF of the positive AMO phase (Fig. 13b, d, f), anomalous cyclones tend to occur east to Baikal, leading to positive precipitation anomalies. Positive precipitation anomalies over the northeastern South America are also reproduced in the AMO_NAI experiments. However, the negative precipitation anomalies in the middle of Australia are not captured the AMO_NAI experiments.

The ECHAM experiments have also captured many precipitation features related to IPO, as shown in Fig. 14. The above analysis reveals that the IPO contributions are mainly in the boreal winter season. Thus, we focus on the DJF season here. During the DJF of the positive phase of IPO (Fig. 14b, d, f), positive precipitation anomalies over southwestern United States, South Asia monsoon

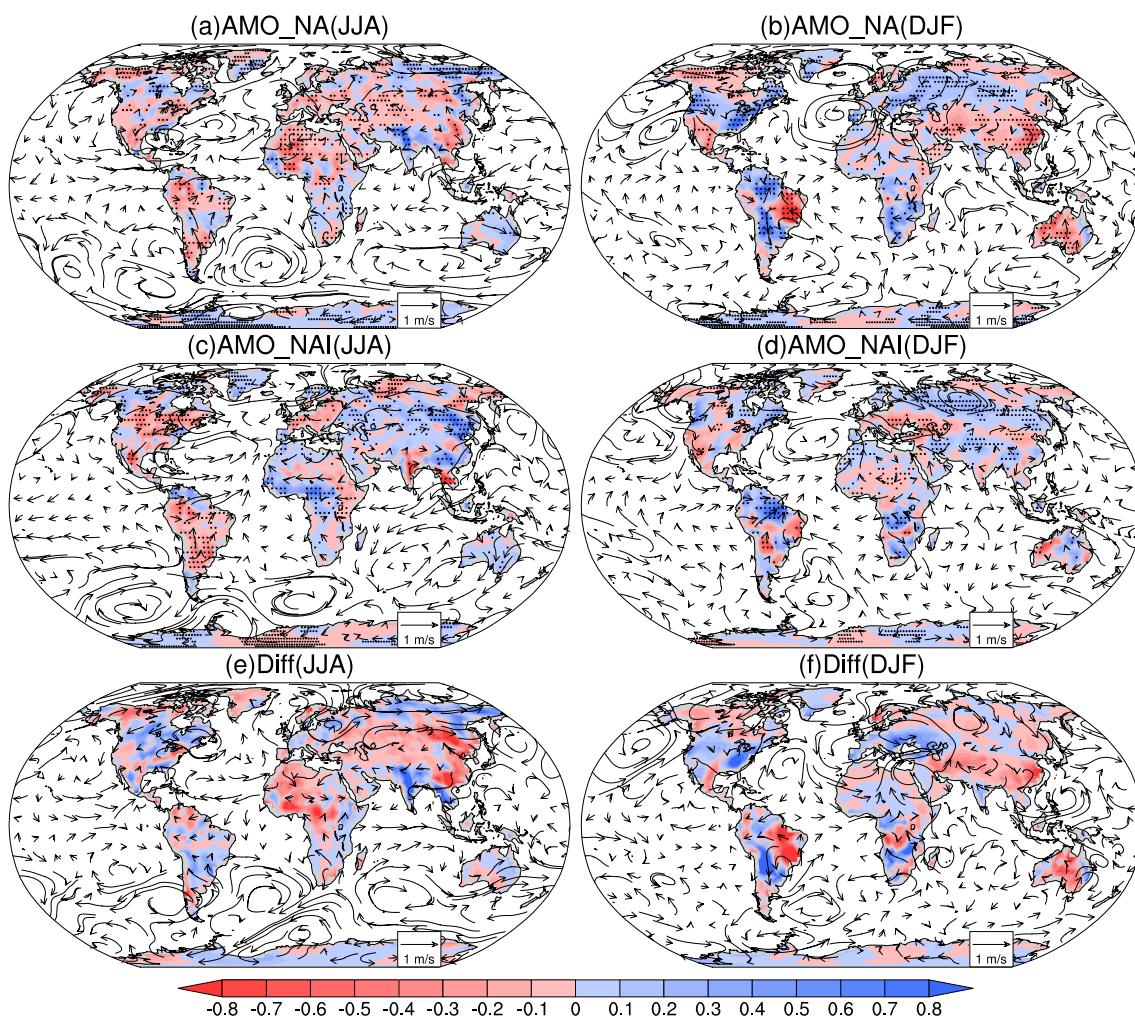


Fig. 13 Simulated precipitation and 850-hPa horizontal winds for the AMO_NA experiment (a, b), the AMO_NAI experiment (c, d), and the differences between them (e, f) for JJA (left column) and DJF (right column). The areas with dots are statistically significant at the

10% level. The AMO_NA experiment refers to the AMO_NA warm run minus the AMO_NA cold run. The AMO_NAI experiment refers to the AMO_NAI warm run minus the AMO_NAI cold run

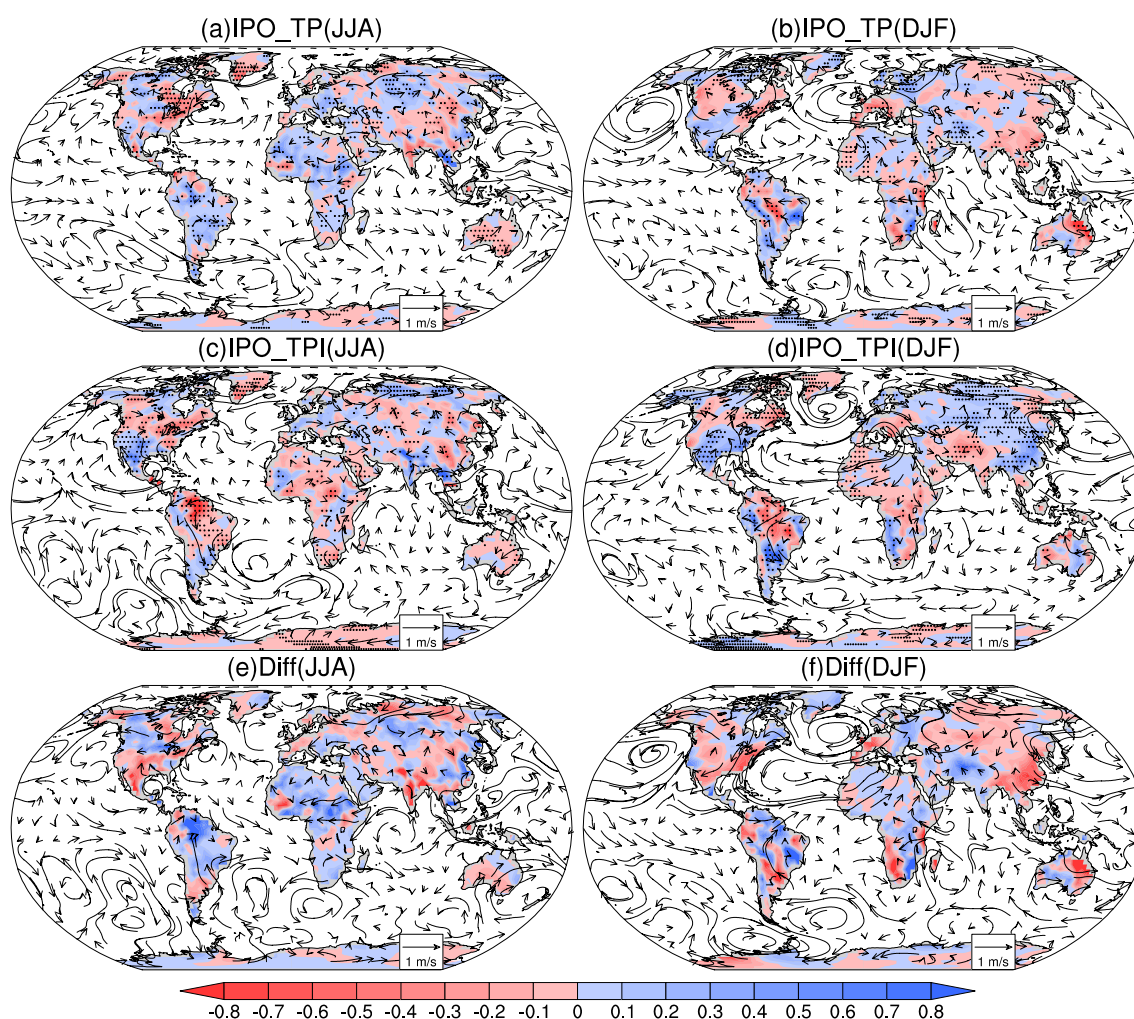


Fig. 14 Simulated precipitation and 850-hPa horizontal winds for the IPO_TP experiment (a, b), the IPO_TPI experiment (c, d), and the difference between them (e, f) for JJA (left column) and DJF (right column). The areas with dots are statistically significant at the 10%

regions, and negative precipitation anomalies over Amazon Basin are well captured in the IPO_TPI run, in good agreement with the precipitation regressed onto the IPO index (Fig. 4f). The IPO_TP run fails to reproduce these important features (Fig. 14b, f), due to a lack of the Indian Ocean SSTA forcing. Though the decadal Indian Ocean basin SSTA is a response to remote forcing from the IPO, with Indian Ocean positive SSTA related to a positive IPO and negative SSTA related to a negative IPO (Han et al. 2014; Dong et al. 2016; Dong and McPhaden 2017a, b), the model results here suggest that the Indian Ocean SSTA affects the land precipitation variation together with IPO. Discrepancies are seen between the regressed precipitation (Fig. 4f) and the results from the IPO_TPI run (Fig. 14d), which fails to reproduce the negative precipitation anomalies in southern Africa and eastern Australia. In a word, the forcing of the Indian Ocean SST anomalies is pivotal

level. The IPO_TP experiment refers to the IPO_TP warm run minus the IPO_TP cold run. The IPO_TPI experiment refers to the IPO_TPI warm run minus the IPO_TPI cold run

for the role of AMO and IPO to take effect in causing the land precipitation variation.

Many studies have also demonstrated that the warming trend in Indian Ocean has important effect on some key regions for AMO and IPO, such as the south Asian monsoon region, Africa, etc. Specifically, Bader and Latif (2003a, b), Hoerling et al. (2003) and Lu (2009) conducted atmospheric general circulation model (AGCM) experiments and found that the warming in Indian Ocean leads to a drying trend in Sahel. Williams and Funk (2011) and Tierney et al. (2013) stressed that the Indian Ocean drives the East African rainfall interdecadal variability by altering the local Walker circulation, whereas the influence from Pacific Ocean is minimal. In addition, the interdecadal variability of the summer rainfall over East Asia is largely influenced by the change of SSTA and convective activity in the tropical Indian Ocean and tropical western Pacific (Hu 1997; Zhou et al. 2009;

etc.). Zhang (2017) suggested that the SST anomalies in the southern Indian Ocean play a crucial role on the interdecadal change of the East Asian summer monsoon, so on and so forth. All these studies substantiate our aforementioned finding that Indian Ocean is pivotal in getting AMO and IPO to work together to cause the precipitation variabilities.

4 Summary

This study has explored the relative contributions of ocean modes to the changes of the JJA and DJF land precipitations during the period 1934–2015. Three dominant modes, namely, GW, AMO and IPO, have been identified through an SVD analysis of the tropical land precipitation between 30° N and 30° S and the SST between 45° N and 20° S. The global precipitation trend is statistically linked to the warming trend of SST. Its interdecadal variation is related to AMO and IPO. Numerical experiments with the ECHAM 4.6 further reveal the effects of Pacific and Atlantic SST anomalies (SSTA), and show that the Indian Ocean SSTA is pivotal for AMO and IPO to take effect in causing the land precipitation variabilities, a fact which has not been reported before.

The relative contributions of GW, AMO and IPO to the global land precipitation variation are further quantitatively assessed. This relative contribution quantification is, to our best knowledge, for the first time. Over tropics, GW plays a dominant role in both JJA and DJF. In JJA, AMO is the second dominant contributor, while IPO becomes so in DJF. The contributions of GW, AMO and IPO to the JJA land precipitation are of the same order with the latitude bands: 10° S–10° N, 50° N–60° N and 40° S–50° S. Outside the bands GW and AMO are the two dominant contributors. In DJF, IPO plays a dominant role between 20° S–40° N. Beyond 20° S–40° N, GW takes over the role. The AMO contribution is smallest between 40° S–50° N.

The three ocean modes have different contributions in different regions (Figs. 6 and 8). The percentage contribution from GW is more than 40% over North America and Asia in JJA, and more than 50% over Europe in DJF. With GW, in JJA, the northeastern North America gets wet, and Asia, except the northwestern China, becomes dry; in DJF, Europe, especially west Europe, Greenland, Scandinavia, South America and west Australia are getting wet, while West Canada, East Russia are getting dry. Africa is getting dry in both seasons.

In JJA, the AMO percentage contribution is more than 40% over northern Africa, Europe, and South America. Positive precipitation anomalies are found over Sahel and Siberia, while negative precipitation anomalies found over South America during the positive phase of AMO. In DJF, the IPO contribution is more than 50% over the southwestern

United States. Northeastern North America and southeastern South America, southern Africa, East Australia, South Asia monsoon region and North China are also affected by IPO. Increased rainfall over the Brazil Plain and North China, decreased rainfall over northeastern South America, southern Africa and East Australia are observed during the positive IPO phase.

The obtained contributions have been cross-validated through information flow analysis, a recently developed tool for causal inference in a rigorous and quantitative sense. Shown in this study are patterns of causalities from GW, AMO, and IPO to the interdecadal precipitation variabilities. Regions sensitive to the three modes have been identified henceforth (in terms of information flow), which are in general consistent with the SVD and regression analysis results.

Acknowledgements This study is supported by the National Key Research and Development Program of China (2016YFA0600402) and the National Natural Science Foundation of China (41630423).

References

- Allen MR, Ingram WJ (2002) Constraints on future changes in climate and the hydrologic cycle. *Nature* 419:224–232. <https://doi.org/10.1038/nature01092>
- Bader J, Latif M (2003a) The impact of decadal-scale Indian ocean sea surface temperature anomalies on Sahelian rainfall and the north Atlantic oscillation. *Geophys Res Lett* 30:2169. <https://doi.org/10.1029/2003GL018426>
- Bader J, Latif M (2003b) The impact of decadal-scale Indian ocean sea surface temperature anomalies on Sahelian rainfall and the north Atlantic oscillation. *Geophys Res Lett* 30:2169–2172. <https://doi.org/10.1029/2003GL018426>
- Baines P, Folland C (2007) Evidence for a rapid global climate shift across the late 1960s. *J Clim* 20:2721–2744. <https://doi.org/10.1175/JCLI4177.1>
- Bretherton CS, Smith C, Wallace JM (1992) An intercomparison of methods for finding coupled patterns in climate data. *J Clim* 5:541–560. [https://doi.org/10.1175/1520-0442\(1992\)005<0541:AIOMFF>2.0.CO;2](https://doi.org/10.1175/1520-0442(1992)005<0541:AIOMFF>2.0.CO;2)
- Cane MA, Clement AC, Kaplan A et al (1997) Twentieth-century sea surface temperature trends. *Science* 275:957–960. <https://doi.org/10.1126/science.275.5302.957>
- Chou C, Neelin JD (2004) Mechanisms of global warming impacts on regional tropical precipitation. *J Clim* 17:2688–2701
- Cole JE, Dunbar R, Mcclanahan T, Muthiga N (2000) Tropical pacific forcing of decadal SST variability in the western indian ocean over the past two centuries. *Science* 287:617–619. <https://doi.org/10.1126/science.287.5453.617>
- Dai A (2013) The influence of the inter-decadal Pacific oscillation on US precipitation during 1923–2010. *Clim Dyn* 41:633–646. <https://doi.org/10.1007/s00382-012-1446-5>
- Dai A, Fung IY (1997) Surface observed global land precipitation variations during 1900–1988. *J Clim* 10:2943–2962
- Dawdy DR, Matalas NC (2020) Statistical and probability analysis of hydrologic data, part III: Analysis of variance, covariance and time series. In: Te Chow V (ed) *Handbook of applied hydrology*. pp 868–890

- Deser C, Phillips A, Hurrell JW (2004) Pacific interdecadal climate variability: linkages between the tropics and the north pacific during boreal winter since 1900. *J Clim* 17:3109–3124
- Dong B, Dai A (2015) The influence of the interdecadal pacific oscillation on temperature and precipitation over the globe. *Clim Dyn* 45:2667–2681. <https://doi.org/10.1007/s00382-015-2500-x>
- Dong L, McPhaden MJ (2017a) The role of external forcing and internal variability in regulating global mean surface temperatures on decadal timescales. *Environ Res Lett* 12:034011. <https://doi.org/10.1088/1748-9326/aa5dd8>
- Dong L, McPhaden MJ (2017b) Why has the relationship between Indian and Pacific Ocean decadal variability changed in recent decades? *J Clim* 30:1971–1983. <https://doi.org/10.1175/JCLI-D-16-0313.1>
- Dong L, Zhou T, Dai A et al (2016) The footprint of the inter-decadal Pacific oscillation in Indian ocean sea surface temperatures. *Sci Rep* 6:21251. <https://doi.org/10.1038/srep21251>
- Emori S, Brown SJ (2005) Dynamic and thermodynamic changes in mean and extreme precipitation under changed climate: mean and extreme precipitation changes. *Geophys Res Lett* 32:L17706. <https://doi.org/10.1029/2005GL023272>
- Folland CK, Palmer TN, Parker DE (1986) Sahel rainfall and worldwide sea temperatures, 1901–1985. *Nature* 320:602–607. <https://doi.org/10.1038/320602a0>
- Greve P, Orlowsky B, Mueller B et al (2014) Global assessment of trends in wetting and drying over land. *Nat Geosci* 7:716–721. <https://doi.org/10.1038/ngeo2247>
- Gromping U (2006) Relative importance for linear regression in R: the package relaimpo. *J Stat Softw* 17:2–27. <https://doi.org/10.18637/jss.v017.i01>
- Gu G, Adler RF (2013) Interdecadal variability/long-term changes in global precipitation patterns during the past three decades: global warming and/or pacific decadal variability? *Clim Dyn* 40:3009–3022. <https://doi.org/10.1007/s00382-012-1443-8>
- Gu G, Adler RF (2015) Spatial patterns of global precipitation change and variability during 1901–2010. *J Clim* 28:4431–4453. <https://doi.org/10.1175/JCLI-D-14-00201.1>
- Han W, Meehl GA, Hu A, Zheng J, Kenigson J, Vialard J, Rajagopalan B (2017) Decadal variability of the indian and pacific walker cells since the 1960s: do they covary on decadal time scales? *J Climate* 30:8447–8468. <https://doi.org/10.1175/JCLI-D-16-0783.1>
- Han W, Vialard J, Mcphaden MJ et al (2014) Indian ocean decadal variability: a review. *Bull Am Meteorol Soc* 95:1679–1703. <https://doi.org/10.1175/BAMS-D-13-00028.1>
- Hansen J, Sato M, Ruedy R et al (2006) Global temperature change. *Proc Natl Acad Sci* 103:14288–14293. <https://doi.org/10.1073/pnas.0606291103>
- Harris I, Jones PD, Osborn TJ, Lister DH (2014) Updated high-resolution grids of monthly climatic observations—the CRU TS3.10 dataset. *Int J Climatol* 34:623–642. <https://doi.org/10.1002/joc.3711>
- Held IM, Soden BJ (2006) Robust responses of the hydrological cycle to global warming. *J Clim* 19:5686–5699. <https://doi.org/10.1175/JCLI3990.1>
- Henley B, Thyer M, Kuczera G (2013) Climate driver informed short-term drought risk evaluation. *Water Resour Res* 49:2317–2326. <https://doi.org/10.1002/wrcr.20222>
- Hoerling M, Kumar A (2003) The perfect ocean for drought. *Science* 299:691–694. <https://doi.org/10.1126/science.1079053>
- Hu Z-Z (1997) Interdecadal variability of summer climate over East Asia and its association with 500 hPa height and global sea surface temperature. *J Geophys Res* 102:19403–19412. <https://doi.org/10.1029/97JD01052>
- John VO, Allan RP, Soden BJ (2009) How robust are observed and simulated precipitation responses to tropical ocean warming? *Geophys Res Lett* 36:L14702. <https://doi.org/10.1029/2009GL038276>
- Kalnay E, Kanamitsu M, Kistler R, et al (1996) The NCEP/NCAR reanalysis 40-year project. *Bull Am Meteorol Soc* 77:437–471
- Kerr RA (2007) A north atlantic climate pacemaker for the centuries. *Science* 288:1984–1985. <https://doi.org/10.1126/science.288.5473.1984>
- Knight JR, Folland CK, Scaife AA (2006) Climate impacts of the atlantic multidecadal oscillation. *Geophys Res Lett* 33:L17706. <https://doi.org/10.1029/2006GL026242>
- Krishnan R, Sugi M (2003) Pacific decadal oscillation and variability of the Indian summer monsoon rainfall. *Clim Dyn* 21:233–242. <https://doi.org/10.1007/s00382-003-0330-8>
- Kushnir Y (1994) Interdecadal variations in north atlantic sea surface temperature and associated atmospheric conditions. *J Clim* 7:141–157
- Liang XS (2014) Unraveling the cause-effect relation between time series. *Phys Rev E* 90:052150. <https://doi.org/10.1103/PhysRevE.90.052150>
- Liang XS (2016) Information flow and causality as rigorous notions ab initio. *Phys Rev E* 94:052201. <https://doi.org/10.1103/PhysRevE.94.052201>
- Lu J (2009) The dynamics of the Indian Ocean sea surface temperature forcing of Sahel drought. *Clim Dyn* 33:445–460. <https://doi.org/10.1007/s00382-009-0596-6>
- Mantua NJ, Hare SR, Zhang Y et al (1997) A pacific interdecadal climate oscillation with impacts on salmon production. *Bull Amer Meteorol Soc* 78:1069–1079
- McCabe GJ, Palecki MA, Betancourt JL (2004) Pacific and Atlantic Ocean influences on multidecadal drought frequency in the United States. *Proc Natl Acad Sci* 101:4136–4141. <https://doi.org/10.1073/pnas.0306738101>
- Meehl GA, Hu A (2006) Megadroughts in the Indian monsoon and southwest North America and a mechanism for associated multi-decadal Pacific sea surface temperature anomalies. *J Clim* 19:1605–1623
- Meehl GA, Hu A, Arblaster JM et al (2013) Externally forced and internally generated decadal climate variability associated with the interdecadal pacific oscillation. *J Clim* 26:7298–7310. <https://doi.org/10.1175/JCLI-D-12-00548.1>
- Mohino E, Janicot S, Bader J (2011) Sahel rainfall and decadal to multi-decadal sea surface temperature variability. *Clim Dyn* 37:419–440. <https://doi.org/10.1007/s00382-010-0867-2>
- Power S, Casey T, Folland C, Colman A, Mehta V (1999) Interdecadal modulation of the impact of ENSO on Australia. *Clim Dyn* 15:319–324. <https://doi.org/10.1007/s003820050284>
- Rayner AN (2011) Global analyses of sea surface temperature, sea ice, and night marine air temperature since the late nineteenth century. *J Geophys Res* 108:4407. <https://doi.org/10.1029/2002JD002670>
- Reason CJC (2002) ENSO-like decadal variability and South African rainfall. *Geophys Res Lett* 29:1638. <https://doi.org/10.1029/2002GL014663>
- Roeckner E et al (1996) The atmospheric general circulation model ECHAM-4: Model description and simulation of present-day climate. Report 218. Max-Planck-Institut für Meteorologie, Hamburg
- Salinger MJ, Renwick JA, Mullan AB (2001) Interdecadal pacific oscillation and south pacific climate. *Int J Climatol* 21:1705–1721. <https://doi.org/10.1002/joc.691>
- Schlesinger ME, Ramankutty N (1994) An oscillation in the global climate system of period 65–70 years. *Nature* 367:723–726. <https://doi.org/10.1038/367723a0>
- Schneider U, Becker A, Finger P et al (2014) GPCC's new land surface precipitation climatology based on quality-controlled in situ data and its role in quantifying the global water cycle. *Theor Appl Climatol* 115:15–40. <https://doi.org/10.1007/s00704-013-0860-x>

- Smith T, Reynolds R, Peterson T, Lawrimore J (2008) Improvements to NOAA's historical merged land-ocean surface temperature analysis (1880–2006). *J Clim* 21:2283–2296. <https://doi.org/10.1175/2007JCLI2100.1>
- Stips A, Macías D, Eayrs C et al (2016) On the causal structure between CO₂ and global temperature. *Sci Rep* 6:21691. <https://doi.org/10.1038/srep21691>
- Tierney JE, Smerdon JE, Anchukaitis KJ, Seager R (2013) Multidecadal variability in East African hydroclimate controlled by the Indian Ocean. *Nature* 493:389–392. <https://doi.org/10.1038/nature11785>
- Verdon D, Wyatt A, Kiem A, Franks S (2004) Multidecadal variability of rainfall and streamflow: Eastern Australia. *Water Resour Res* 40:W10201. <https://doi.org/10.1029/2004WR003234>
- Wilcox LJ, Highwood EJ, Dunstone NJ (2013) The influence of anthropogenic aerosol on multi-decadal variations of historical global climate. *Environ Res Lett* 8:024033. <https://doi.org/10.1088/1748-9326/8/2/024033>
- Williams AP, Funk C (2011) A westward extension of the warm pool leads to a westward extension of the Walker circulation, drying eastern Africa. *Clim Dyn* 37:2417–2435. <https://doi.org/10.1007/s00382-010-0984-y>
- Wu Z, Huang N (2009) Ensemble empirical mode decomposition: a noise-assisted data analysis method. *Adv Adapt Data Anal* 1:1–41. <https://doi.org/10.1142/S1793536909000047>
- Xie S, Deser C, Vecchi GA et al (2010) Global warming pattern formation: sea surface temperature and rainfall. *J Clim* 23:966–986. <https://doi.org/10.1175/2009JCLI3329.1>
- Yang Q, Ma Z, Fan X et al (2017) Decadal modulation of precipitation patterns over eastern china by sea surface temperature anomalies. *J Clim* 30:7017–7033. <https://doi.org/10.1175/JCLI-D-16-0793.1>
- Zeng-Zhen Hu (1997) Interdecadal variability of summer climate over East Asia and its association with 500 hPa height and global sea surface temperature. *J Geophys Res Atmos*. <https://doi.org/10.1029/97jd01052>
- Zhang H, Wen Z, Wu R et al (2017) Inter-decadal changes in the East Asian summer monsoon and associations with sea surface temperature anomaly in the South Indian Ocean. *Clim Dyn* 48:1125–1139. <https://doi.org/10.1007/s00382-016-3131-6>
- Zhang R, Delworth TL (2006) Impact of Atlantic multidecadal oscillations on India/Sahel rainfall and Atlantic hurricanes. *Geophys Res Lett* 33:L17712. <https://doi.org/10.1029/2006GL026267>
- Zhang X, Zwiers FW, Hegerl GC et al (2007) Detection of human influence on twentieth-century precipitation trends. *Nature* 448:461–465. <https://doi.org/10.1038/nature06025>
- Zhang Y, Wallace JM, Battisti DS (1997) ENSO-like interdecadal variability: 1900–1993. *J Clim* 10:1004–1020
- Zhou T, Yu R, Zhang J et al (2009) Why the western pacific subtropical high has extended westward since the Late 1970s. *J Clim* 22:2199–2215. <https://doi.org/10.1175/2008JCLI2527.1>

Publisher's Note Springer Nature remains neutral with regard to jurisdictional claims in published maps and institutional affiliations.